ELSEVIER

Journal of Alloys and Compounds 217 (1995) 273–282

Journal of ALLOYS AND COMPOUNDS

Phase diagram of the Pr–Fe–B system

A.C. Neiva [a], A.P. Tschiptschin [b], F.P. Missell [a]

[a] *Instituto de Física, Universidade de São Paulo, CP 20516, 01452-990 São Paulo, SP, Brazil*

[b] *Escola Politécnica, Universidade de São Paulo, CP 8174, 01065-970 São Paulo, SP, Brazil*

Received 25 March 1994; in final form 18 July 1994

Abstract

The Pr–Fe–B phase diagram was determined in the low boron regions of the ternary system. It is presented and discussed in terms of four vertical sections, a polythermic projection and a Scheil diagram. Six ternary invariant reactions are found in the region investigated: a peritectic maximum, a eutectic maximum, three transition reactions, and a degenerate reaction. The final solidification sequence, with the degenerate reaction, can also be applied to Nd–Fe–B.

Keywords: Phase diagrams; Ternary systems

1. Introduction

The compound $Pr_2Fe_{14}B$ possesses magnetic properties similar to those of $Nd_2Fe_{14}B$, allowing, in principle, the fabrication of Pr–Fe–B and Pr–Nd–Fe–B magnets with excellent characteristics. However, the magnetic properties of a permanent magnet depend not only on the intrinsic properties of the principle phase, but also on the microstructure of the magnet. An important tool for the control of the microstructure is the phase diagram of the system. For this reason, in recent years, many studies of the phase diagrams of Nd–Fe–B have been presented. Pr–Fe–B stable and metastable phase equilibria have been also studied [1,2], but the Pr–Fe–B phase diagram is relatively unknown. The object of the present work is to present and discuss this diagram in terms of four vertical sections, a polythermic projection and a Scheil diagram.

Three ternary phases are known for Pr–Fe–B: ϕ ($Pr_2Fe_{14}B$), η ($Pr_{1+x}Fe_4B_4$), and ρ ($Pr_5Fe_2B_6$). Their structural and magnetic characteristics are presented in Table 1. Table 2 presents the phases of the boundary systems Pr–Fe, Pr–B, and Fe–B.

2. Compositions studied and experimental procedure

The compositions studied are presented in Table 3 and in Fig. 1, which also shows the phase fields studied for each sample after a long homogenizing anneal and the positions of the four vertical sections obtained.

The region covered by these studies includes the solidification sequence corresponding to the compositions which seem most adequate for the production of Pr–Fe–B permanent magnets by powder metallurgy techniques, in the light of experience with Nd–Fe–B magnets. These compositions are close to that of the ϕ phase, with a certain excess of Pr. The solidification sequence could involve Fe (which one tries to avoid), the η phase, the Pr_2Fe_{17} (2:17) phase, and finally the phases Pr, A_1, and A_1'. The ferromagnetic A_1 and A_1' phases are metastable [11,12] and are not presented on the diagram or in Tables 1 and 2. They form fine eutectics A_1+Pr and $A_1'+Pr$ from the final Pr-rich liquid in the solidification of both Pr–Fe–B and Pr–Fe alloys. Similar phases (as shown by Mössbauer spectra [13]) in Nd–Fe have a composition around 34 at.% Nd.

The vertical sections examined in greatest detail are A and B. The first corresponds to the beginning of solidification. It includes the pseudobinary section Fe–ϕ and is intended for studying the peritectic reaction $L+Fe \rightarrow \phi$. The vertical section B, on the contrary, corresponds to the end of solidification. It shows the invariant reactions which generate the three-phase fields $\phi+Pr+\eta$ and $\phi+Pr+2{:}17$.

The samples were prepared in an arc furnace from electrolytic Fe (purity, 99.98%), Pr ingot (99.9%), and B pieces (99.8%). The alloy buttons were turned and remelted several times to guarantee homogeneity. Maximum weight losses admitted during fusion were 0.1%. Occasional inhomogeneous samples, as revealed by their

Elsevier Science S.A.
SSDI 0925-8388(94)01356-X

Table 1
Crystallographic and magnetic properties of ternary Pr–Fe–B phases

Phase	Pearson symbol, space group, and prototype	Lattice parameters (pm)	Comments	Magnetic properties
$Pr_2Fe_{14}B$ (ϕ phase)	tP68 $P4_2/mnm$ $Nd_2Fe_{14}B$ [3]	$a=880.3$ $c=1223.2$ [3]		$T_C=570$ K [3] $M_S=137.2$ e.m.u. g^{-1} [4] $H_A=59$ kOe [3]
$Pr_{1+x}Fe_4B_4$ ($x=0.106$) [5] (η phase)	$I4/mmm$ (A) $P4_2/ncm$ (B) $Nd_{1.1}Fe_4B_4$ [5]	$a=715.8$ $c_A=353.01$ $c_B=390.42$ [5]	2 sublattices: A, Pr atoms; B, Fe–B pairs [5]	$T_C=7.5$ K [6]
$Pr_5Fe_2B_6$ (ρ phase)	$R3m$ $Pr_5Co_2B_6$ [6]	$a=548.1$ $c=2433$ [6]		

Table 2
Crystallographic and magnetic properties of Pr–Fe, Pr–B, and Fe–B phases

Phase and temperature range (K)		Pearson symbol, space group, and prototype		Lattice parameters (pm)		Magnetic properties		Comments	
α-Pr $\leqslant 1068$	[7]	hP4 $P6_3/mmc$ α-La	[7]	$a=367.21$ $c=1183.26$	[7]				
β-Pr 1068–1204	[7]	cI2 $Im3m$ W	[7]	$a=413$	[7]				
β-B 1138–2365	[7]	hR105 $R3m$ β-B	[7]	$a=1017$ $\alpha=65.12°$	[7]				
α-Fe $\leqslant 1185$	[7]	cI2 $Im3m$ W	[7]	$a=286.65$	[7]	$T_C=1044$ K	[7]		
γ-Fe 1185–1667	[7]	cF4 $Fm3m$ Cu	[7]	$a=364.67$	[7]				
δ-Fe 1667–1811	[7]	cI2 $Im3m$ W	[7]	$a=293.13$	[7]				
Pr_2Fe_{17} $\leqslant 1378$		hR19 $R3m$ Th_2Zn_{17}	[8]	$a=858.5$ $c=1246.3$	[8]	$T_C=283$ K	[8]	Other prototype: Nb_2Be_{17}	[9]
PrB_x ($x<4$)	[7]							Pr_2B_5, monoclinic	[9]
PrB_4 $\leqslant 2623$	[10]	tP20 $P4/mbm$ ThB_4	[10]	$a=724.1$ $c=411.9$	[10]	$T_C=25$ K	[9]		
PrB_6 $\leqslant 2883$	[10]	cP7 $Pm3m$ CaB_6	[10]	$a=413.27$	[10]	$T_N=7$ K	[9]		
FeB $\leqslant 1923$	[10]	oP8 $Pnma$ FeB	[10]	$a=550.6$ $b=295.2$ $c=406.1$	[10]			Other space group: $Pbmn$	[7]
Fe_2B $\leqslant 1662$	[10]	tI12 $I4/mcm$ Cu_2Al	[10]	$a=511.0$ $a=424.9$	[10]				

Table 3
Compositions of Pr–Fe–B samples

Sample number	Composition (at.%)			Solid phases	Vertical section
	Pr	Fe	B		
1	5	92.5	2.5	ϕ+Fe	A
2	10	85	5	ϕ+Fe	A and C
3	13.2	80.2	6.6	$\phi+\eta$+Pr	A
4	17.8	73.3	8.9	$\phi+\eta$+Pr	A
5	60	38.2	1.8	ϕ+Pr+2:17	B
6	60	37.3	2.7	ϕ+Pr	B
7	60	36.8	3.2	$\phi+\eta$+Pr	B and C
8	60	26.6	13.4	$\phi+\eta$+Pr	B
9	60	23.3	16.7	$\phi+\eta$+Pr	B
10	60	20	20	η+Pr	B
11	22.3	73.3	4.4	ϕ+Pr+2:17	C
12	48.1	48.4	3.5	ϕ+Pr+2:17	
13	11.6	73.3	15.1	$\phi+\eta$	D
14	80	15	5	$\phi+\eta$+Pr	

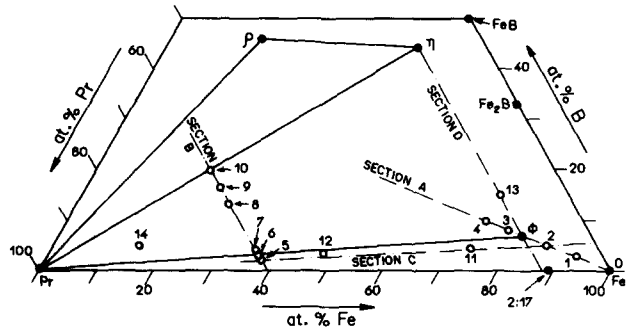

Fig. 1. Compositions studied and positions of the four vertical sections.

microstructures, were not studied. Afterwards, the samples were wrapped in Ta foil and sealed in Ar-containing silica tubes for annealing. The samples were maintained at 873 K for 30 days and then quenched into water. Some samples were also annealed at 1273 K in the same manner. Observations of the as-cast and annealed materials were carried out by optical metallography using a Neophot microscope with polarized light. Quantitative energy-dispersive spectroscopy (EDS) analyses were made using a Cambridge Stereoscan 240 scanning electron microscope. Phase identification was complemented by X-ray diffraction and magnetic measurements using a vibrating sample magnetometer. Differential thermal analysis (DTA) was carried out using a Netzsch 404S thermal analyser, with heating and cooling rates of both 5 and 10 K min^{-1}. The samples were wrapped in Ta foil to avoid Al pick-up from the alumina crucibles. No Ta or Al contamination was detected by EDS analyses.

3. Phase diagram

3.1. Liquidus projection and reaction sequence

Fig. 2 presents the polythermic projection and Fig. 3 the corresponding Scheil diagram. Six ternary invariant reactions are proposed in these diagrams. They are discussed in the items which treat the four vertical sections studied: Max.p_1 is discussed in Section 3.2, U_2 and U_3 in Section 3.3, U_1 in Section 3.4, and Max.e_1 in Section 3.5. The polythermic projection exhibits six regions of primary solidification corresponding to Fe, 2:17, Pr, ρ, η, and ϕ. Their boundaries, the univariant liquid lines, are mostly represented as broken lines, because the equilibrium liquid compositions were estimated for the invariant reactions. These univariant lines are also represented in the lower parts of Figs. 4, 6, 9 and 13, which present the four vertical sections.

3.2. Vertical section A

In terms of the final solid phases, the vertical section A begins at the Fe vertex, enters the field Fe+ϕ, passes through ϕ, and finally enters the field $\phi+\eta$+Pr. The section includes samples 1–4 and corresponds to compositions where the Pr:B ratio is equal to 2. The

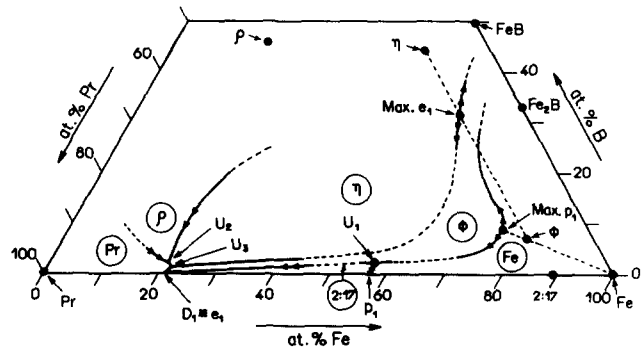

Fig. 2. Polythermic projection with the liquidus curves.

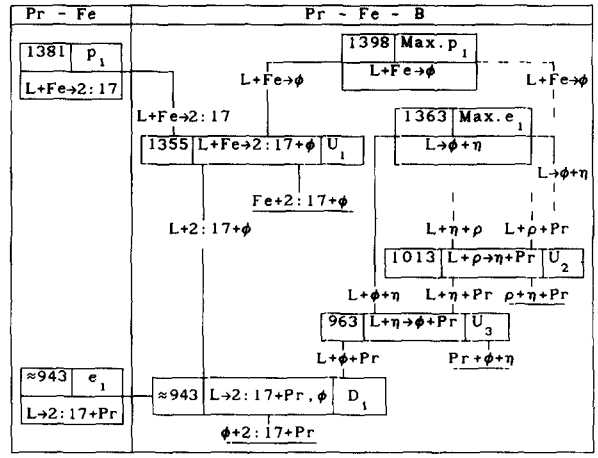

Fig. 3. Scheil diagram (temperatures in kelvins).

section proposed is presented in Fig. 4. It exhibits a pseudobinary peritectic reaction $L+Fe \rightarrow \phi$ (the maximum Max.p_1) around 1398 K.

The peritectic character of the reaction was determined from the microstructures of the as-cast samples 1, 2, and 3, which are typical of peritectic reactions (Fig. 5 shows the as-cast microstructure of sample 2). In these samples, we observed primary Fe surrounded by the ϕ phase, with additional phases (Pr, η and possibly A_1 and A_1') in the grain boundaries. In samples 1 and 2, these additional phases are metastable with respect to solid state equilibria. In sample 3, the metastable phase is Fe. In both cases, the metastable microstructure is explained in terms of an interruption of the peritectic reaction. In sample 4, primary Fe is not observed. For this reason the peritectic composition of the liquid was taken to be intermediate between those of samples 3 and 4.

The temperatures represented on the figure by upwardly directed triangles correspond to thermal events on the DTA heating curves for these samples. These temperatures are about 20 K higher than the equivalent events observed on the cooling curves. The equilibrium temperatures must lie between these two values, closer to the heating curve.

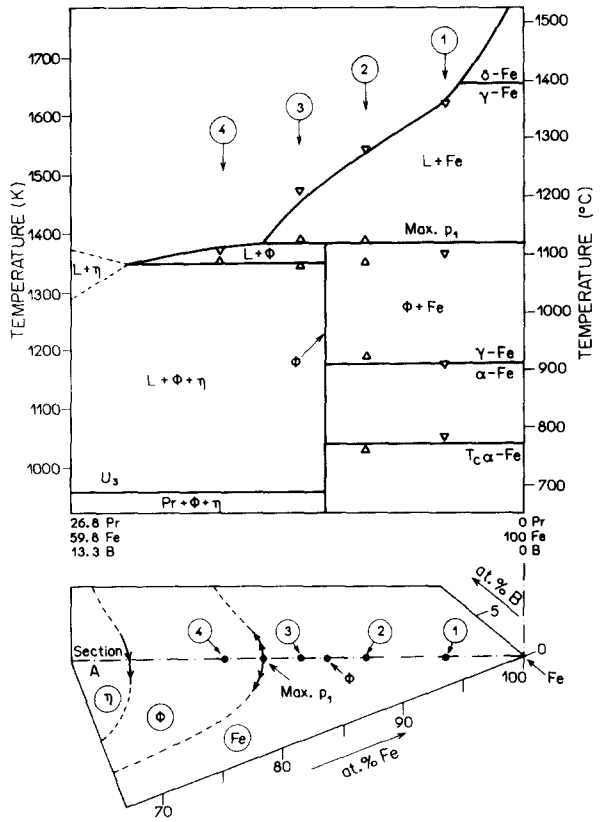

Fig. 4. Vertical section A (above) and part of the composition triangle (below), with the polythermic projection of the univariant lines.

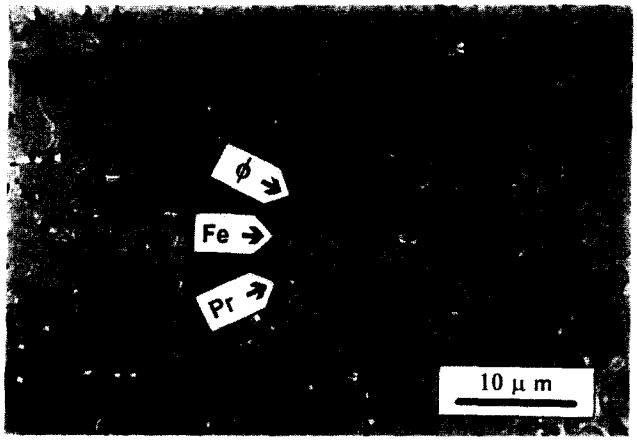

Fig. 5. Microstructure of sample 2, as-cast (polarized light): primary phase, Fe; secondary phase, ϕ; tertiary phase, Pr. Magnetic domains can be observed in the ϕ phase. Other additional phases, as η, A_1, and A_1', are not easily distinguished in this region of the sample.

3.3. Vertical section B

The vertical section B corresponds to compositions with 60 at.% Pr. It begins at binary Pr–Fe (solid field 2:17+Pr), enters the region 2:17+Pr+ϕ, passes through Pr+ϕ, enters Pr+ϕ+η, passes through Pr+η, and terminates in the field ρ+Pr+η. The section proposed is presented in Fig. 6.

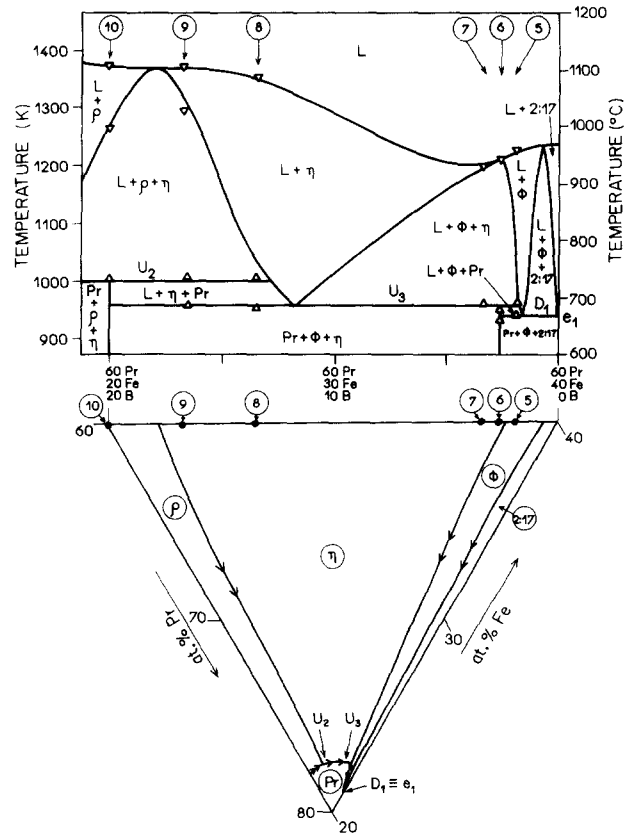

Fig. 6. Vertical section B (above) and part of the composition triangle (below), with the polythermic projection of the univariant lines.

3.3.1. The liquidus curve

The liquidus curve of vertical section B was determined from the temperatures of the initial events of the DTA cooling curves and was subdivided into the primary fields identified by the microstructures of the as-cast samples 5, 6, 7, 8, 9, and 10, as indicated in Table 4. In this table, the term "proinvariant" phase is used in the same sense as proeutectic or properitectic phase. That is, the phases referred to are precipitated from a liquid in bivariant (such as $L \rightarrow \phi$) or univariant (such as $L \rightarrow \phi + \eta$) reactions which precede an invariant reaction (for example, the invariant reaction including the phases L, ϕ, η, and Pr). Since we do not know, in principle, whether this invariant reaction is eutectic or peritectic or transition, we use the more general term proinvariant.

3.3.2. The invariant reactions

The invariant reactions of vertical section B were defined principally on the basis of the thermal events observed during the heating of annealed samples in the DTA. These events are indicated on the vertical section. The corresponding curves, as well as those of some other samples which do not belong to the section, are presented in Fig. 7. We wish to comment on certain aspects of these curves.

3.3.2.1. The events at 943 and 963 K

The two samples of the field $2{:}17+\phi+Pr$ present two events at low temperatures (about 943 and about 963 K), while the four samples of the field $\phi+\eta+Pr$ present only one event, that at 963 K. The event at 963 K is attributed to a transition reaction (U_3), which gives rise to the solid field $\phi+\eta+Pr$ and to the univariant line $L+\phi+Pr$. This line descends to the invariant reaction at 943 K (D_1), which gives rise to the field $2{:}17+\phi+Pr$.

3.3.2.2. The events around 943 K: the degenerate equilibrium

The events at lower temperatures for the samples of the field $2{:}17+\phi+Pr$ (samples 5 and 11) were observed at temperatures close to the low temperature event of the binary sample Pr–78 at.% Fe:

Equilibrium	Sample	DTA Event
$L+2{:}17+Pr$	Pr–78 at.% Fe	946 K
$L+2{:}17+Pr+\phi$	11	950 K
$L+2{:}17+Pr+\phi$	5	941 K

These two equilibria must be connected by the line $L+2{:}17+Pr$. The temperature difference between these two equilibria, however, is less than the uncertainty in the measurements, so that it is not possible to say which one occurs at a higher temperature. In other words, it is not possible to determine whether the equilibrium $L+2{:}17+Pr+\phi$ is eutectic (having the lower temperature) or transition (having the higher temperature). There exists, of course, a third possibility: a eutectic maximum $L \rightarrow 2{:}17+Pr$, giving rise to two lines $L \rightarrow 2{:}17+Pr$. Each of these lines would terminate in one of the invariant equilibria in question. This option would be more general than the other two in the sense that it would permit any relation between the temperatures and could be consistent with final liquids being rich or poor in boron, in the triangle $2{:}17+\phi+Pr$. However, this option is slightly artificial since it would introduce a new reaction (the eutectic maximum) without any supporting experimental evidence.

The experimental results do not permit a decision as to the nature of the ternary reaction. However, it is reasonable to assume that the final liquid is poor in boron, in the light of the similarities in microstructure of the as-cast binary and ternary samples, on the one hand, and of the fact that the temperatures of the two

Table 4
Proinvariant phases observed in as-cast samples

Sample	Proinvariant phases	Probable primary phase
5	ϕ	ϕ
6	$\phi+\eta$	η
7	$\phi+\eta$	η
8	$\phi+\eta$	η
9	$\eta+\rho$	? (η or ρ)
10	$\eta+\rho$	? (η or ρ)

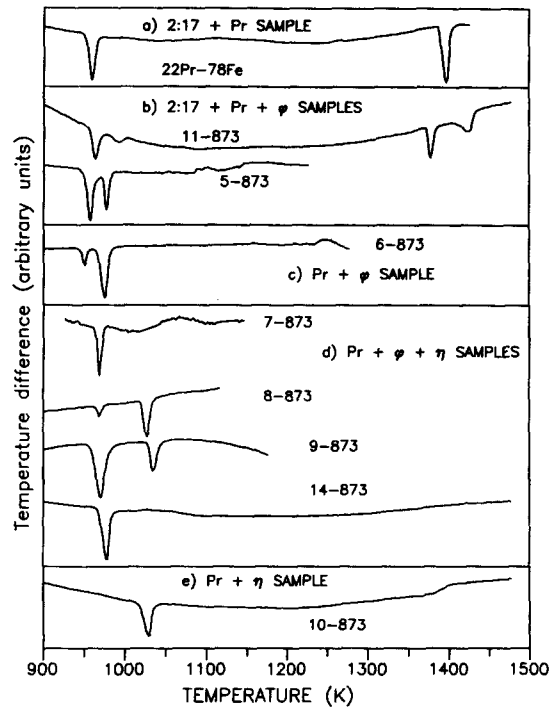

Fig. 7. DTA heating curves for Pr–Fe–B samples annealed at 873 K for 30 days. Heating rate, 5 K min^{-1}.

reactions are very close to each other, on the other hand. This ternary reaction, therefore, must be capable of representing this low boron content and also the proximity of the temperatures.

For these reasons, we adopted another representation of this reaction: the ternary equilibrium L + 2:17 + ϕ + Pr is considered to be neither a eutectic nor a transition equilibrium, but instead a degenerate equilibrium. The degenerate equilibrium is a limiting situation between a eutectic and a peritectic equilibrium in a binary system, or between a eutectic and a transition equilibrium in a ternary system. In this case, one of the constituents, although it is in equilibrium with the rest, has an insignificant participation in the corresponding reaction. Clearly the term insignificant is relative. In the present case, a few hundred parts per million of B could, in first approximation, be considered insignificant, being, as well, below the detection limits usually encountered in the analysis of microregions. Thus, it is assumed that the phases 2:17, Pr, and L do not contain boron. The phase which would have insignificant participation would be ϕ, the only one containing a significant amount of boron. Without the formation or dissolution of ϕ, no flux of boron would occur in the reaction, a necessary condition in view of the absence of boron in the remaining phases. The ternary region L + 2:17 + Pr, having its origin in the binary system, degenerates to a line belonging to the binary.

3.3.2.3. The event at 1013 K

An event was observed at 1013 K in samples 8, 9, and 10. It was attributed to the transition reaction L + $\rho \rightarrow \eta$ + Pr (U_2). This reaction connects the line L + η + ρ, whose existence was proposed on the basis of microstructural evidence (see Table 4), to the line L + η + Pr, whose existence is necessary as one of the origins of reaction U_3, at 963 K (discussed in Section 3.3.2.1). The reaction U_2 presupposes the existence of the line L + ρ + Pr and the solid field $\rho + \eta$ + Pr. These were not observed experimentally, since they require sample compositions which were not studied.

3.4. Vertical section C: the origin of the univariant field ϕ + 2:17 + L

During the determination of vertical section B, we verified the existence of a field L + ϕ + 2:17, which deserved a more detailed examination. Starting from the Pr–Fe binary system, one might imagine that this field originates in the field L + 2:17 + Fe, which, in turn, originates in the binary peritectic equilibrium. With the addition of boron, the liquid would rapidly become saturated with ϕ, which does not have a high boron content (5.9 at.%), establishing an equilibrium L + 2:17 + Fe + ϕ. This hypothesis is reinforced by the fact that the univariant liquid line L + 2:17 + ϕ is located close to the binary Pr–Fe, i.e. is poor in boron, at least in the region of vertical section B (60 at.% Pr).

At 1355 K, sample 11-873 (composition 11, annealed at 873 K) presents a very sharp endothermic event, typical of invariant reactions, on the DTA heating curve. Sample 2-1273 also presents this event, weakly but clearly. The heating curves for these two samples are shown in Fig. 8. The temperature of these endothermic events, 1355 K, is slightly below that of the binary peritectic reaction, 1381 K. For this reason, we propose a transition reaction at 1355 K, which receives a univariant line from the binary peritectic. This reaction is presented in vertical section C, shown in Fig. 9.

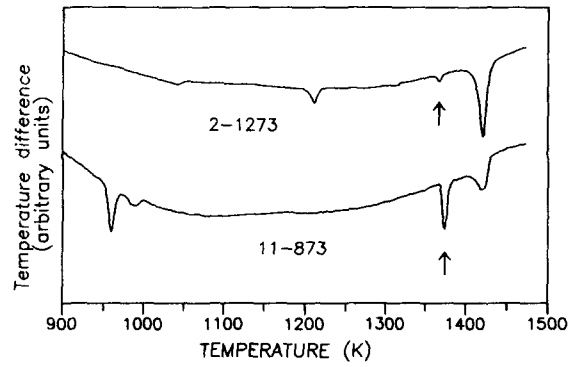

Fig. 8. DTA heating curves for sample 2, annealed at 1273 K, and sample 11, annealed at 873 K. The arrows indicate the events around 1355 K. Heating rate, 5 K min^{-1}.

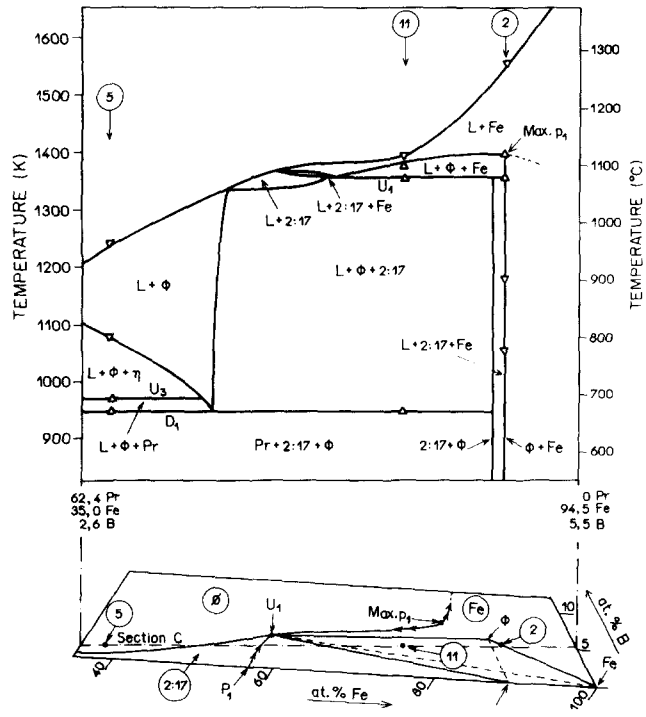

Fig. 9. Vertical section C (above) and part of the composition triangle (below), with the polythermic projection of the univariant lines. This version supposes that the composition of the liquid participating in U_1 is richer in boron than the line corresponding to the vertical section.

The proposed reaction must necessarily receive the univariant line L+ϕ+Fe. This line originates in the pseudobinary peritectic Max.p_1. The reaction should also generate a solid field Fe+2:17+ϕ. This field would, in principle, be outside the range of compositions studied. However, the DTA event at 1355 K in sample 2-1000 shows that its composition did not exactly match the line Fe+ϕ, as expected, but actually lies in the three-phase field Fe+2:17+ϕ. The reduced intensity of the event observed in this sample is consistent with the small quantity of 2:17 present.

3.5. *Vertical section D: the origin of the univariant field L+ϕ+η*

Apart from the univariant field L+2:17+ϕ discussed in the previous section, another important univariant field was predicted in vertical section B: L+ϕ+η. In the Nd–Fe–B system, it was verified that the line L+ϕ+η originates in the pseudobinary eutectic L→ϕ+η [14,15]. A similar hypothesis will be considered in the case of Pr–Fe–B.

In the present study, composition 13 belongs to the field ϕ+η. The microstructure of sample 13 after DTA solidification, shown in Fig. 10, presents primary Fe, secondary ϕ, a ϕ+η eutectic and a small quantity of Pr. Both Fe and Pr are metastable with respect to solid state equilibria.

The DTA heating curve of the annealed sample ϕ+η (with insignificant amounts of Fe and Pr remaining), shown in Fig. 11, presents a strong endothermic event at 1363 K, followed by a series of ill-defined events. The strong event can be ascribed to the invariant reaction ϕ+η→L. If the sample belonged to the field of primary crystallization of ϕ or η, one should observe no sharp events above the invariant reaction (since the crossing of the liquidus line should correspond just to the end

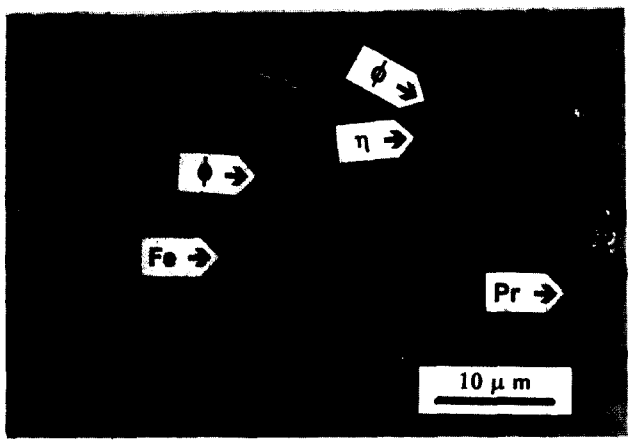

Fig. 10. Microstructure of sample 13, after DTA cooling (5 K min^{-1}) (polarized light): primary phase, Fe; secondary phase, ϕ; tertiary phases, ϕ+η; quaternary phase, Pr. Magnetic domains can be observed in some ϕ grains.

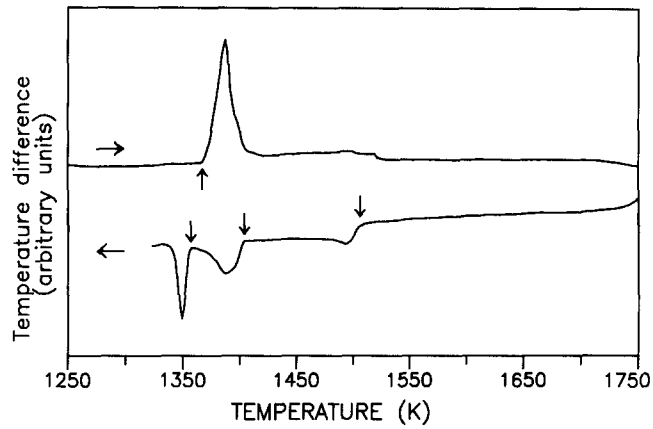

Fig. 11. DTA heating and cooling curves for sample 13, annealed at 1273 K.

of ϕ→L or η→L). As shown by the microstructure, however, the sample belongs to the field of primary crystallization of Fe. Therefore, the reactions leading to the formation of Fe above the invariant reaction can explain those ill-defined events observed on heating.

On cooling, three exothermic events are observed above 1363 K. The first, at about 1500 K, should be ascribed to L→Fe. The second, at about 1395 K, should be ascribed to the formation of ϕ, observed in the microstructure as a secondary phase. It may therefore be ascribed to the univariant reaction L+Fe→ϕ, which originates at the invariant reaction Max.p_1 (Section 3.2), at 1398 K.

The system being in equilibrium or not, the reaction that follows univariant L+Fe→ϕ should be L→ϕ, because of the extinction (if equilibrium had been attained) or isolation (as observed in this sample) of the Fe. The transition from L+Fe→ϕ to L→ϕ, however, should not induce a sharp DTA event, but rather a slight change in inclination. Therefore, the third cooling event, at about 1360 K, should not be ascribed to this transition, but rather to the subsequent reaction, L→ϕ+η. A question then arises that can be discussed with the help of Fig. 12: is this reaction the invariant reaction observed during heating, or is it the univariant reaction L→ϕ+η? The observed temperature of this event is near that of the invariant reaction observed on heating, thus suggesting that the invariant equilibrium has also been observed during cooling. However, the presence of Fe in the final microstructure indicates that the liquid which had undertaken the reaction L→ϕ was richer in Pr than the liquid of equilibrium L→ϕ. Since the equilibrium liquid should follow the line that links ϕ to η, thus arriving at the invariant composition, this non-equilibrium liquid should arrive at the univariant line L→ϕ+η, which then proceeds to Pr-rich compositions, rather than to the invariant point. The presence of Pr in the final microstructure confirms this hypothesis. We should note, however, that the com-

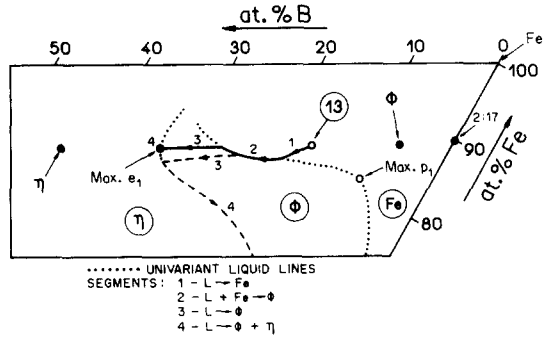

Fig. 12. Partial polythermic projection with schematic solidification liquid paths for sample 13. Equilibrium solidification (——) corresponds to the complete dissolution of the primary Fe. Non-equilibrium solidification (– – –) corresponds to the interruption of the univariant reaction $L+Fe \rightarrow \phi$ before Fe is completely consumed.

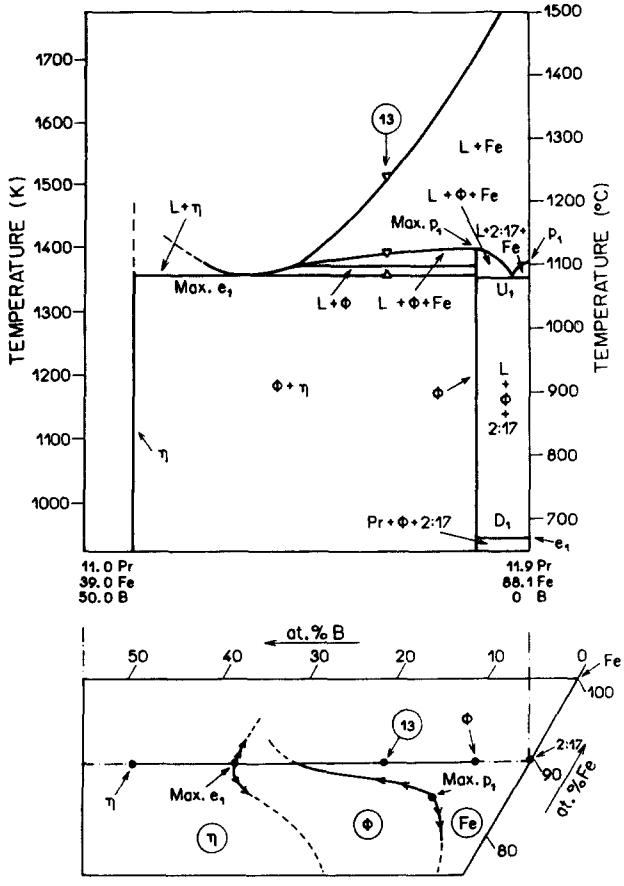

Fig. 13. Vertical section D (above) and part of the composition triangle (below), with the polythermic projection of the univariant lines.

position of the initial liquid of this reaction may have been near the invariant composition, because the amounts of the phases Fe and Pr observed in the microstructure were relatively small.

A schematic presentation of the pseudobinary ϕ–η is shown in Fig. 13. The eutectic composition corresponds to $x_\eta/x_\phi = 0.7$. This value is arbitrary, and was taken from the x_η/x_ϕ value observed in the eutectic of the DTA sample (estimated from quantitative metallography), which, as mentioned above, was formed during a univariant reaction. The third DTA event observed in the cooling, at 1360 K (Fig. 11), was not plotted, because, as discussed above, it does not correspond to the equilibrium reaction.

4. Comparison with Nd–Fe–B

The Pr–Fe–B phase diagram obtained shows a great similarity to that of Nd–Fe–B. The reaction sequence presented by Stadelmaier et al. [16] for the region of the Nd–Fe–B diagram corresponding to alloys rich in Fe exhibits high temperature reactions similar to those proposed here: a peritectic maximum $L+Fe \rightarrow \phi$, a eutectic maximum $L \rightarrow \phi+\eta$, and a transition reaction $L+Fe \rightarrow \phi+Nd_2Fe_{17}$. These reactions were verified in subsequent, more complete, work [14,15,17].

The final solidification sequences presented there [14–17] differ among those publications and differ, as well, from that presented here. More recently, however, Landgraf et al. [18–20] presented a revision of the final solidification sequence. It displays four principal differences in relation to previous versions: (a) the univariant liquid line $L+\phi+\eta$ corresponds to low boron contents (which was confirmed by Knoch et al. [21]); (b) the field $\phi+\eta+Nd$ is formed in a transition reaction (U_{15}) from which the line $L+\phi+Nd$ goes toward lower boron contents; (c) the field $2:17+\phi+Nd$ is formed in a reaction where the liquid has a low boron content; (d) the final reaction giving rise to $2:17+\phi+Nd$ occurs at a temperature which is indistinguishable from that of the binary eutectic $L \rightarrow \phi+Nd$.

These four features were also observed in Pr–Fe–B. However, the Pr–Fe–B phase diagram presented here differs from that presented by Landgraf et al. in that the final reaction for the formation of $2:17+\phi+Pr$ is considered to be a degenerate invariant reaction, that is, a reaction in which one of the phases participating in the equilibrium (in this case, ϕ) does not participate actively in the reaction. Given the great similarity between the final reactions in the two systems, it would not be unreasonable to suppose that the reaction which forms $2:17+\phi+Nd$ in Nd–Fe–B is also a degenerate reaction, described by $L \rightarrow 2:17+Nd, \phi$. For comparison of the two systems, Fig. 14 presents the Scheil diagram of Nd–Fe–B, according to Landgraf [20], with the final solidification reactions from his study and the higher temperature reactions as determined in previous studies. In Table 5, we compare the corresponding reactions in the two systems.

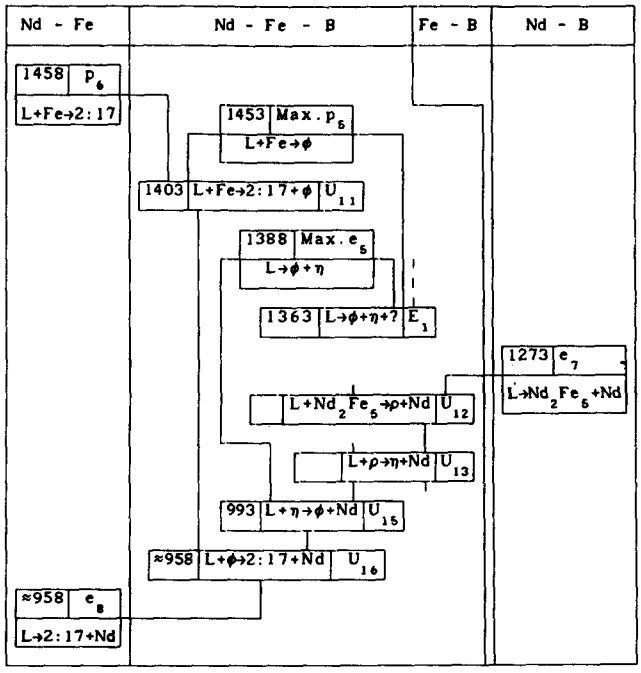

Fig. 14. Scheil diagram for Nd–Fe–B (temperatures in kelvins). See Refs. [18–20].

Table 5
Equivalent reactions of the Nd–Fe–B and Pr–Fe–B diagrams

Nd–Fe–B		Pr–Fe–B	
Reaction	T (K)	Reaction	T (K)
p_6	1458	P_1	1381
Max.p_5	1453	Max.p_1	1398
U_{11}	1403	U_1	1355
Max.e_5	1388	Max.e_1	1363
U_{13}	–	U_2	1013
U_{15}	993	U_3	963
U_{16}	≈958	–	–
–	–	D_1	≈943
e_8	≈958	e_1	≈943

5. Kinetics of formation of ϕ in the solid state

Sample 14 (Pr–15 at.% Fe–5 at.% B) belongs to the field $\phi+\eta+$Pr. In the as-cast form, however, it does not present the phases ϕ and η, but instead the phases A_1, A_1', and ρ. After annealing at 873 K, these phases are replaced by ϕ and η. A mere 10 min anneal at 873 K is sufficient to eliminate the Curie event associated with A_1 (around 498 K) in favour of that associated with ϕ (563 K).

A similar situation occurs in the system Nd–Fe–B [22]. To compare the kinetics of this process in the two systems, 873 K annealings were carried out for different times. The formation of ϕ was followed in terms of the coercivity of the samples. With the formation of ϕ, H_c increases, since this phase has a greater magnetocrystalline anisotropy than A_1 or A_1'. With increasing grain size, however, H_c begins to decrease. Fig. 15 presents these results. We note that the Nd alloy attains high coercivity values in shorter times.

It should be stressed that these H_c values cannot be compared as absolute values, since Pr–Fe–B samples were measured at room temperature, while Nd–Fe–B samples were measured at 368 K. When measured at room temperature, Nd–Fe–B alloys exhibited higher coercivities (above 18 kOe, for the 10–100 min annealings) than Pr–Fe–B samples. This can be explained by differences in the initial grain size of the ϕ particles.

However, independent of the differences observed, these results bring out an important point: high coercivities are attained in both cases with annealings whose duration is comparable with that used in post-sintering heat treatments of $R_2Fe_{14}B$ magnets. The compositions of these samples, rich in Pr or Nd, are close to those of the intergranular regions in sintered magnets. The elimination of a low coercivity intergranular phase (A_1) results in increased coercivity in the magnet.

The difference between the kinetics of the Nd- and Pr-containing alloys may be of more general significance. Neiva et al. [13,23] observed that the formation of the Nd_5Fe_{17} phase in heat treatments at 873 K became much slower with the partial substitution of Pr for Nd. The Nd_5Fe_{17} (5:17) phase (hexagonal, $P6_3mcm$, $T_C=503$ K, basal anisotropy, formed peritectically between 1043 and 1068 K [24]) is not present in as-cast samples. In Fe-rich compositions with up to 89.5 at.% Fe the as-cast samples reveal 2:17, Nd, and A_1. With annealing treatments, 2:17, A_1, and Nd dissolve into 5:17. For samples Nd–70 at.% Fe, and annealings at 873 K, 5:17 is almost completely formed (i.e. just a small amount of 2:17 is still present) after 720 h, and it is completely

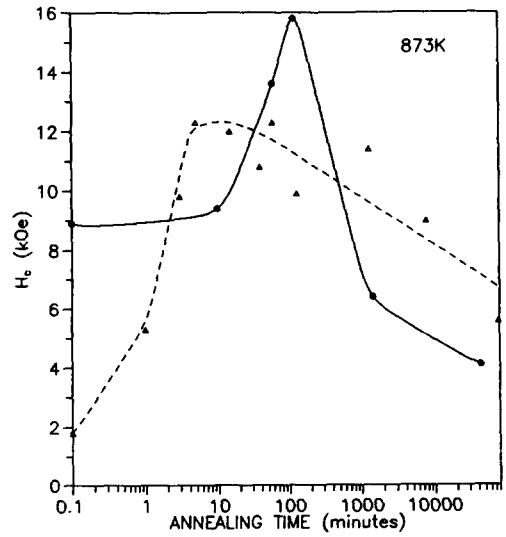

Fig. 15. Coercive field H_c as a function of annealing time for Pr–15 at.% Fe–5 at.% B (—) and Nd–15 at.% Fe–5 at.% B (– – –). The data for the Nd–Fe–B sample are from Ref. [22]. The Pr data were obtained at 300 K, while the Nd data correspond to 368 K.

formed after 1440 h. If half the Nd is substituted by Pr, no 5:17 is noticeable after 720 h, and just a small amount is noticeable after 1440 h. In terms of the production of magnets, all these results suggest that longer annealing times may be necessary in magnets containing Pr.

6. Conclusions

The phase diagram of Pr–Fe–B was obtained and presented in terms of four vertical sections, a polythermic projection, and a Scheil diagram. Six invariant ternary reactions were encountered: a peritectic maximum, a eutectic maximum, three transition reactions and a degenerate reaction. The phase diagram of Pr–Fe–B presents great similarities to that of Nd–Fe–B and the microstructures of Pr–Fe–B and Nd–Fe–B samples are found to be very similar, in both the as-cast and the annealed (873 K) condition. For this reason, the final solidification sequence proposed here, involving a degenerate reaction, should also be applicable to Nd–Fe–B. Thus, the general principles governing the fabrication of Nd–Fe–B magnets should also be applicable to Pr–Fe–B and Nd–Pr–Fe–B magnets. Considering the slower kinetics in the case of Pr–Fe–B alloys, the annealing of Pr–Fe–B magnets must be longer than that of their Nd counterparts.

Acknowledgements

The authors wish to thank F.J.G. Landgraf for many useful discussions. The technical assistance of S.A. Romero, S. Silva, D.A.P. Bulla, and V.I. dos Santos is acknowledged. This work was supported by CNPq, FINEP–PADCT, and FAPESP. A.C. Neiva acknowledges a doctoral fellowship from CAPES.

References

[1] H.H. Stadelmaier, N.A. Elmasry and S. Cheng, *Mater. Lett., 2* (1983) 169–172.
[2] F.A.O. Cabral, *Thesis,* Universidade Estadual de Campinas, 1991.
[3] C. Abache and H. Oesterreicher, *J. Appl. Phys., 57* (1985) 4112–4114.
[4] Y.-C. Yang, H.-Y. Chen, Z.-X. Liu, B. Liao, F. Xing and W.-W. Ho, *J. Appl. Phys., 57* (1985) 4115–4117.
[5] A. Bezinge, H.F. Braun, J. Muller and K. Yvon, *Solid State Commun., 55* (1985) 131–135.
[6] O.M. Dub, N.F. Chaban and Y. B. Kuz'ma, *J. Less-Common Met., 117* (1986) 297–302.
[7] T.B. Massalski, *Binary Alloy Phase Diagrams,* American Society for Metals, Metals Park, OH, 2nd edn., 1990.
[8] K.H.J. Buschow, *Rep. Prog. Phys., 40* (1977) 1179–1256.
[9] K.H.J. Buschow, in E.P. Wohlfarth (ed.), *Ferromagnetic Materials,* Vol. 1, Elsevier, Amsterdam, 1980.
[10] P. Villars and L.D. Calvert, *Pearson's Handbook of Crystallographic Data for Intermetallic Phases,* American Society for Metals, Metals Park, OH, 1985.
[11] A.C. Neiva, T. Yonamine, F.J.G. Landgraf and F.P. Missell, in S. G. Sankar (ed.), *Proc. 6th Int. Symp. on Magnetic Anisotropy and Coercivity in Rare Earth–Transition Metal Alloys,* Carnegie Mellon University, Pittsburgh, PA, 1990, pp. 236–249.
[12] A.C. Neiva, *Thesis,* Universidade de São Paulo, 1993.
[13] H.R. Rechenberg, F.J.G. Landgraf, A.C. Neiva, R. Politano and F.P. Missell, *Mater. Lett., 14* (1992) 21–26.
[14] Y. Matsuura, S. Hirosawa, H. Yamamoto, S. Fujimura, M. Sagawa and K. Osamura, *Jpn. J. Appl. Phys., 24* (1985) L635–L637.
[15] G. Schneider, E.-Th. Henig, G. Petzow and H.H. Stadelmaier, *Z. Metallkd., 77* (1986) 755–761.
[16] H.H. Stadelmaier, N.A. Elmasry, N.C. Liu and S.F. Cheng, *Mater. Lett., 2* (1984) 411–415.
[17] T.S. Chin, D.S. Tsai, Y.H. Chang, S.E. Hsu and M.P. Hung, in C. Herget, H. Kronmüller and R. Poerschke (eds.), *Proc. 5th Int. Symp. on Magnetic Anisotropy and Coercivity in Rare Earth–Transition Metal Alloys, Bad Soden, 1987,* Vol. II, Bad Soden, 1987, p. 403.
[18] F.J.G. Landgraf, F.P. Missell, G. Knoch, B. Grieb and E.-Th. Henig, *J. Appl. Phys., 70* (1991) 6107–6109.
[19] F.J.G. Landgraf, *Thesis,* Universidade de São Paulo, 1992.
[20] F.J.G. Landgraf, personal communication.
[21] K.G. Knoch, B. Reinsch and G. Petzow, *Z. Metallkd., 85* (1994) 350–353.
[22] G. Schneider, F.J.G. Landgraf and F.P. Missell, *J. Less-Common Met., 153* (1989) 169–180.
[23] A.C. Neiva, F.J.G. Landgraf and F.P. Missell, *J. Alloys Comp., 190* (1992) 69–72.
[24] F.J.G. Landgraf, G. Schneider, V. Villas-Boas and F.P. Missell, *J. Less-Common Met., 163* (1990) 209–218.